ADJOINT STATE METHOD FOR THE IDENTIFICATION PROBLEM IN SPECT: RECOVERY OF BOTH THE SOURCE AND THE ATTENUATION IN THE ATTENUATED X-RAY TRANSFORM

SONGTING LUO, JIANLIANG QIAN, AND PLAMEN STEFANOV

Abstract. Motivated by recent theoretical results obtained by the third author for the identification problem arising in single-photon emission computerized tomography (SPECT), we propose an adjoint state method for recovering both the source and the attenuation in the attenuated X-ray transform. Our starting point is the transport-equation characterization of the attenuated X-ray transform, and we apply efficient fast sweeping methods to solve static transport equations and adjoint state equations. Numerous examples are presented to demonstrate various features of the identification problem, such as uniqueness and non-uniqueness, stability and instability, and recovery of the wave front set.

1. Introduction

We study the attenuated X-ray transform in the plane arising in single-photon emission computerized tomography (SPECT):

$$X_a f(x,\theta) = \int e^{-Ba(x+t\theta,\theta)} f(x+t\theta)\, dt, \quad x \in \mathbf{R}^2,\ \theta \in S^1, \tag{1}$$

with a source $f(x)$ and an attenuation $a(x)$ that we want to recover. Here,

$$Ba(x,\theta) = \int_0^\infty a(x+t\theta)\, dt \tag{2}$$

is the "beam transform" of a, usually denoted by Da. We assume that both attenuation a and source f are compactly supported. The experimental setup for SPECT is the following: radioactive markers are injected into a patient's body and the emitted gamma rays, attenuated by the body, are detected outside of the body. Since the measured emitted radiation reflects both the distribution of the emitter and the attenuation, the purpose is to reconstruct the source (the distribution of the emitter) with an unknown attenuation coefficient. In clinical applications, additional transmission measurements have to be taken to reconstruct a first [27], and eliminating or reducing those additional measurements remains an important problem [27, 5].

Mathematically, the problem we study is the following: can we recover both f and a knowing $X_a f$? It is sometimes called the identification problem for SPECT. The answer in general is negative; for example if $f = 0$, we cannot recover a. When the attenuation a is identically zero, the attenuated X-ray transform reduces to the ordinary X-ray transform; when the attenuation a is a constant on a convex set containing the support of f, then the attenuated X-ray transform reduces to the so-called exponential X-ray transform. When the attenuation a is known, f can be reconstructed uniquely even by means of explicit formulas [6, 1], [21, 22], [20, 11].

Date: October 2, 2013.

Second author partly supported by NSF. Third author partly supported by a NSF Grant DMS-0800428.

Recovery of both a and f simultaneously from $X_a f$ is a much harder problem and there has not been much progress in the mathematical understanding of the identification problem so far. A related but not identical problem for finding both a constant attenuation and the source in the exponential X-ray transform has been studied in [25]. The main result in [25] can be stated that specific pairs of constant a and radial f cannot be distinguished but all others pairs can. The identification problem has also been studied in [18, 19, 3, 2] under the assumption that f consists of finitely many delta sources, and those results do not imply uniqueness; the problem has also been studied in [7] by assuming that a is a constant multiple of the characteristic function of a star-shaped domain. Range conditions [21, 22] have been viewed as a possible tool for solving the problem both numerically [4, 5, 27] and analytically [2].

Although mathematically it is not always clear whether both a and f can be recovered simultaneously uniquely and stably, numerically one can always formulate the inverse problem as an abstract operator equation with both a and f as unknowns and appeal to a certain regularization strategy to stabilize the possible ill-posedness. This approach has been tried in various settings with limited success in [8, 17, 23, 12, 28]. In [8], a direct approach is proposed to discretize the attenuated X-ray transform by treating both attenuation and source as unknowns, and a constrained optimization method is applied to solve the resulting nonlinear system. In [10, 12], Tikhonov regularization methods have been applied to deal with the abstract operator equation resulting from the inverse problem of recovering both a and f, and numerical results have been shown to demonstrate the feasibility of the approach in certain situations. In this work, we also aim at recovering both a and f from the boundary measurement of emission data by inverting $X_a f$ as a system for (a, f), but our approach is based on applying the adjoint state method to the transport-equation characterization of $X_a f$, which is different from the works in [8, 12]; moreover, our approach is largely motivated by the recent theoretical results obtained by the third author in [26].

The third author studied the problem in [26] and found conditions under which (a, f) can be recovered even in a stable way. Complete theoretical understanding of this problem is still lacking, and we do not have if and only if conditions for uniqueness and for stability. The goal of this work is tri-fold: firstly, to develop an efficient numerical approach and in particular, to demonstrate the non-uniqueness and instability in some cases and the uniqueness and stability in other; secondly, to validate the theory developed in [26] and to study examples for which the theory is not complete yet; thirdly, to demonstrate numerically which part of the wave front set (describing in particular jumps across curves) of a and f can be recovered in the fully nonlinear setting of the inverse problem. The theoretical understanding of recovering the wave front set of a and f is much more complete in the linearized setting as shown in [26], see Theorem 2.2, and Theorem 2.3 below.

2. Theoretical background

In this section, we review some of the results in [26]. Assume that a and f are supported in some smooth domain Ω. Set

$$\Gamma_{\pm} = \{(x, \theta) \in \partial\Omega \times S^1 : \ \pm\theta \cdot n(x) \geq 0\},$$

where $n(x)$ is the unit outer normal to $\partial\Omega$. The operator $X_a f$ can be also characterized as follows. Let $u(x, \theta)$ solve the transport equation

$$(\theta \cdot \nabla + a(x, \theta))u(x, \theta) = f(x, \theta), \quad u|_{\Gamma_-} = 0. \tag{3}$$

Then

$$X_a f = u|_{\Gamma_+}.$$

The transport equation is sometimes more convenient to work with than formula (1). To linearize near some background (a, f), denote by δa and δf the perturbations of a and f, and by δu the perturbation of u. Then we get

$$(\theta \cdot \nabla + a)\delta u + (\delta a)u = \delta f, \quad \delta u|_{\Gamma_-} = 0. \tag{4}$$

This implies

$$\delta u|_{\Gamma_+} = \delta X_a(\delta f, \delta a) = X_a \delta f - I_{e^{-Ba}u}\delta a. \tag{5}$$

Here and below, I_w denotes the X-ray transform with weight $w(x, \theta)$. In particular, $X_a = I_{e^{-Ba}}$, thus

$$\delta X_a(\delta f, \delta a) = I_{e^{-Ba}}\delta f - I_{e^{-Ba}u}\delta a. \tag{6}$$

2.1. **Non-uniqueness for radial pairs.**

Theorem 2.1 ([26])**.** *Let $a \in C_0^\infty$ and $f \in C_0^\infty$ be radial. Then there exists a radial $f_0 \in C_0^\infty$ so that*

$$X_a f = X_0 f_0. \tag{7}$$

The smoothness requirement is too strong, and can be weakened considerably. In fact, given f and a, one can find f_0 in an explicit form by computing certain Abel type of integral; see [26]. We have a similar result for the linearized map δX_a as well.

The theorem does not say that for any radial pair we have infinite many pairs with the same data. It does provide an example however of infinite many radial pairs, including those with $a \neq 0$, with the same data. In the numerical example shown in Figure 1, we start with radial (a, f) with $a \neq 0$, and the reconstruction suggests non-uniqueness even in that case, with the result strongly depending on the initial guess.

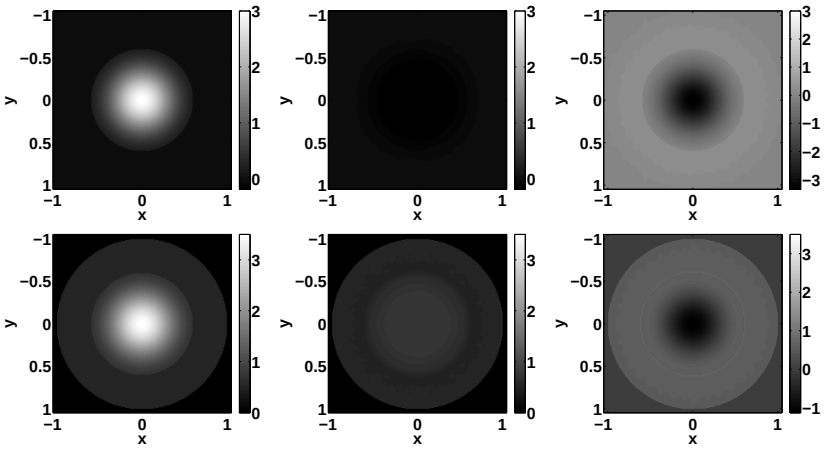

FIGURE 1. Non-uniqueness for radial (a, f). Top row: a, bottom row: f. First column: exact a and f; second and third column: computed with different guesses.

The non-uniqueness for radial a and f affects the problem when (a, f) are close to radial, as shown in Figure 2, We choose the background (a, f), as well as the initial guesses to be as in Figure 1, and perturb (a, f) with small phantoms. Different initial guesses lead to totally wrong background (a, f) as before and the phantoms are not recovered well either.

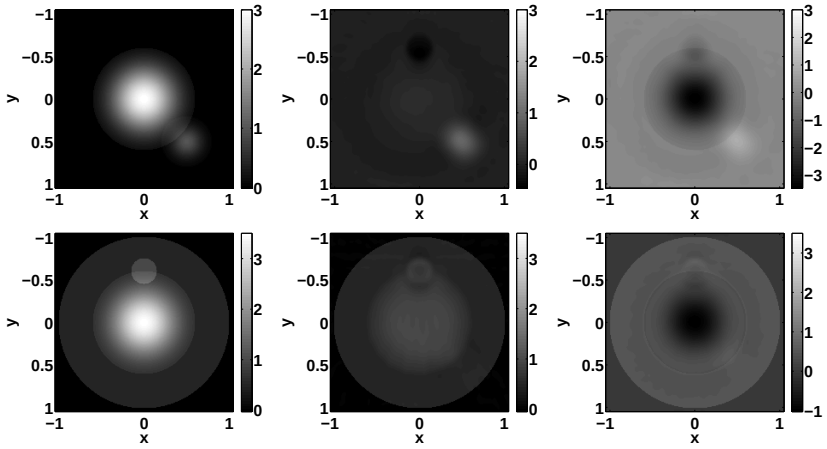

FIGURE 2. Ill-posedness for perturbed radial (a, f). Top row: a, bottom row: f. First column: exact a and f; second and third column: computed with the same different guesses as in Figure 1.

2.2. **Microlocal properties of the linearization.** Most of the analysis in [26] is about the microlocal properties of δX_a. We are first interested in which part of the wave front sets $\mathrm{WF}(\delta a)$ and $\mathrm{WF}(\delta f)$ can be recovered. The wave front sets, in particular, describe the curves over which those functions jump and the size of those jumps.

2.2.1. *Reducing the problem to a 2×2 pseudo-differential system.* If a is known and smooth, then it is well known that $X_a f$ given on an open family of lines determines in a stable way $\mathrm{WF}(f)$ on the conormals to those lines. Note that in X_a and in δX_a defined in (5), we integrate over each line twice: once in each direction. Loosely speaking, this is a system of two equations for two unknowns. In fact, we can write it as a 2×2 pseudo-differential system for $(\delta a, \delta f)$ with the principal part

$$\begin{pmatrix} -e^{-Ba}u & e^{-Ba} \\ -e^{-JBa}Ju & e^{-JBa} \end{pmatrix} (x, \xi^{\perp}/|\xi|) \tag{8}$$

where u is the solution to the problem (3), and $(x, \xi^{\perp}/|\xi|) = (x, \theta)$. Here we denote

$$v^{\perp} := (-v_2, v_1), \quad v = (v_1, v_2) \in \mathbf{R}^2, \qquad Ju(x, \theta) := u(x, -\theta).$$

2.2.2. *Microlocal invertibility based on ellipticity.* To determine $\mathrm{WF}(\delta a)$ and $\mathrm{WF}(\delta f)$ at some point $(x, \xi) \in T^*R^n \setminus 0$ by ellipticity, we need to make sure that the determinant of that system is not zero. That determinant turns out to be given by $\tilde{W}(x, \xi^{\perp})$, where

$$\tilde{W}(x, \theta) = -e^{-Ba}e^{-JBa}W, \quad W := u - Ju,$$

extended for convenience to a positively homogeneous function of θ of degree 1. Therefore, up to an elliptic factor, $\tilde{W}$ coincides with

$$W(x, \theta) = u(x, \theta) - u(x, -\theta).$$

This is intuitively clear as well. When $W(x, \theta) = 0$, the weights in equation (6) at x are equal in the directions θ and $-\theta$. Then $\delta X_a(\delta a, \delta f)(x, \theta)$ and $\delta X_a(\delta a, \delta f)(x, -\theta)$ "provide the same information" for δa and δf (microlocally, at (x, ξ)) and the system is degenerate then. Therefore, $W(x, \xi^{\perp}) \neq 0$ is a sufficient condition for microlocal invertibility. In the examples below, we sometimes call the zeros

of W "instability directions" even though the actual stability or instability at them depends on other factors, as we explain below. When there is actual instability at those directions, jumps over curves having those directions at x would be unstably reconstructed. Therefore, the first practical test that we apply to each configuration is to identify those "instability directions" at each point based on some choice of approximate "background" a and f; this is where we can expect (not always!) unstable recovery of jumps. Figure 11 and Figure 13 visualize that; there we can work directly with the actual f and choose the background a to be zero.

We use the following notion of stable reconstruction of wave front sets. Letting U be an open conic set in $T^*R^n \setminus 0$, we say that we can stably reconstruct $\mathrm{WF}(f)$ in U from Af, with A a linear operator, if for any conically compact set $K \Subset U$ and any s_1 there is s_2 so that

$$\|\chi f\|_{H^{s_1}} \leq C_{s_3} \left(\|Af\|_{H^{s_2}} + \|f\|_{H^{s_3}} \right), \quad \forall s_3,$$

where $\chi = \chi(x, D)$ is a zero order pseudo-differential operator (ΨDO) with $\chi = 1$ on K. Such estimates are typically implied by parametrix constructions; see also estimate (26.1.5) in [13] and the argument leading to it. For a slightly different definition using seminorms, we refer to [24]. When such an estimate holds, we say that we can recover f from Af with the loss (or gain) of $s_2 - s_1$ derivatives if that number is positive (or negative). Note that this definition ignores the order of the operator A. In the theorem below, the estimate is sharp, and in that case, there is no actual loss. Going back to the linearized transform, it is of order $-1/2$ as an Fourier Integral Operator (FIO). The proof of the microlocal invertibility is to show that $(\delta X_a)^* \delta X_a$ is a ΨDO of order -1. The loss is therefore $1/2$, the same as in the X-ray transform case, and in this sense, the theorem below gives a sharp result.

Theorem 2.2. *Let $W(x_0, \xi_0^\perp) \neq 0$. Then in a conic neighborhood of (x_0, ξ_0), $\mathrm{WF}(\delta a)$ and $\mathrm{WF}(\delta f)$ can be stably reconstructed from $\delta X_a(\delta a, \delta f)$ with a loss of $1/2$ derivative.*

In Theorem 2.3 below, we show that under a weaker non-trapping condition we can still recover $\mathrm{WF}(\delta a)$ and $\mathrm{WF}(\delta f)$ but with loss of $3/2$ derivatives.

2.2.3. *Microlocal invertibility with loss of one more derivative under a non-trapping condition.* A closer look at the function W reveals that it is odd w.r.t. θ. Then for any x, there are at least two characteristic directions θ at which $W(x, \theta) = 0$ and therefore at least two characteristic co-directions ξ at which $W(x, \xi^\perp) = 0$. Then W cannot be elliptic over any set in Ω. The following non-degeneracy condition guarantees that the characteristic co-directions form a finite set at a given x_0:

$$W(x_0, \theta) = 0 \quad \Longrightarrow \quad \partial_{\theta^\perp} W(x_0, \theta) \neq 0, \quad \forall \theta \in S^1. \tag{9}$$

If (x, ξ) is characteristic, then this still does not mean that we cannot recover the wave front sets at that point in a stable way. The following classical example illustrates that: the operator $\partial/\partial x_1$ is not elliptic, and $(x, (0, \xi'))$ are all characteristic codirections, where $\xi' = (\xi_2, \ldots, \xi_n)$. On the other hand, if we a priori know that $\operatorname{supp} f$ is compact, we can recover f from $\partial f/\partial x_1$ just by integrating over lines in the x_1 direction, starting from points outside $\operatorname{supp} f$. We do not gain or lose derivatives (i.e., $s_1 = s_2$ here) but since that operator is of order 1, and we do not gain a derivative, we may count this as a loss. Note that this recovery of singularities is not local like with the ellipticity argument.

The analog of this example in our situation appears when we consider the Hamiltonian flow of $W(x, \xi^\perp)$ on the zero energy level. The Hamiltonian vector field can be degenerate; for example,

it can be zero in open sets. It is of *real principal type* in Ω (i.e., $dW(x,\xi^\perp)$ is not collinear to ξdx on $W(x,\xi^\perp)=0$; in other words, the Hamiltonian field of W is not radial) if and only if

$$W,\ \theta\cdot\partial_x W,\ \partial_{\theta^\perp} W \text{ cannot be all zero at the same time for any point in } \Omega\times S^1. \tag{10}$$

If $W(x,\xi^\perp)$ is of real principal type, then so is the matrix ΨDO (8); see [9]. For our purpose, the theory of ΨDOs with a scalar real principal type principal symbol will suffice, however. Then microlocally, the operator $W(x,D^\perp)$ is equivalent to $\partial/\partial x_1$. We can still recover the singularities in a given compact set K if the Hamiltonian flow eventually leaves K. If so, we call K non-trapping. Note that we are not gaining a derivative in this construction. The analysis in [26] also shows that we need the non-trapping condition only for $\operatorname{supp} a$ since the problem is elliptic for δf.

Theorem 2.3. *If condition* (10) *holds at* $(x_0,\xi_0^\perp)$ *and if the Hamiltonian curve through* (x_0,ξ_0) *leaves the compact set (where* δa *is a priori supported) at least in one of the two directions, then in a conic neighborhood of* (x_0,ξ_0), $\mathrm{WF}(\delta a)$ *and* $\mathrm{WF}(\delta f)$ *can be stably reconstructed from* $\delta X_a(\delta a,\delta f)$ *with a loss of* $3/2$ *derivatives.*

An example of artifacts along trapped (closed) Hamiltonian curves is presented in Figure 6. In Figure 7, we show how the problem is stabilized if we use the a priori information that δa is in a non-trapping set.

2.2.4. *When the ellipticity and the non-trapping conditions fail.* When the non-trapping condition is not fulfilled, the unrecoverable (stably) singularities can only lie on the characteristic variety $W(x,\xi^\perp)=0$. Note that the flow being trapping does not necessarily imply no stable recovery since the behavior depends on the lower order terms then. The matrix ΨDO (8) has rank at least one all the time so a certain one-dimensional space should be recoverable. In fact, this is related to the polarization set in [9]. As shown in [26], we can recover the wave front set of a certain linear combination stably when (9) holds microlocally.

Proposition 2.1. *Fix* $(x_0,\theta_0)\in\mathbf{R}^2\times S^1$. *Let* $W_0(x_0,\theta_0)=0$ *and* $\partial_{\theta^\perp}W_0(x_0,\theta_0)\neq 0$. *Let*

$$v(x)=u(x,\theta(x)),\quad \text{for } x \text{ near } x_0, \tag{11}$$

where $\theta(x)$ *is the unique local solution of* $W_0(x,\theta)=0$ *with* $\theta(x_0)=\theta_0$, *and* u *is defined by* (3). *Then we can recover the wave front set of*

$$v\delta a-\delta f \tag{12}$$

near $(x_0,\pm\theta_0^\perp)$ *with a loss of* $1/2$ *derivative.*

Since f and therefore, u, is non-negative in applications, we get that errors in the reconstruction of δa, microlocally, must appear as errors of the same sign in the reconstruction of δf, multiplied by v. The statement of the proposition remains true even when equation (3) does not hold but then v is the ΨDO, $v=W(x,D^\perp/|D|)$. This follows directly from (8). Therefore, jumps across smooth curves at characteristic codirections, for example, are related by (12) with v equal to $W(x,\theta)$ with $\theta=\nu^\perp$, where ν is the unit normal to the curve. This can be seen in our numerical examples below, for example, in Figure 8 and Figure 9.

Condition (10) may fail in a whole neighborhood of some $(x_0,\xi_0^\perp)$. Then the Hamiltonian flow can just possibly change the length of ξ_0 and nothing else; its projection on $\mathbf{R}^2\times S^1$, however, does not change. One extreme example of this is when $W=0$ for x in an open set and all directions. This can happen if f is the characteristic function of the region between two concentric ellipses, and x is in the interior of the smaller one. Then δX_a is smoothing on that set and no point of

the wave front set of $(\delta a, \delta f)$ with x there can be stably recovered. The quantity (12) still can be stably recovered however.

Examples illustrating this type of instability are shown in Figure 8 and Figure 9.

2.2.5. *Explanation of the "crosstalk" artifacts.* In our numerical reconstructions, as well as in those in previous papers [10], one can see that "phantoms" (relatively well localized perturbations of a smoothly varying background) in a can appear in the reconstructed f, with different amplitude, and vice versa. This phenomenon can be explained by our analysis. If we think of the phantoms as approximate singularities (with densities approximating functions with jumps across smooth curves, for example), then we can recover (12) or at least its singularities in a stable way, see also the remark in the paragraph below (12). If we cannot recover stably δa and δf, as explained above, this means that we can have relatively large errors in the reconstructed δa and δf, but those errors are of the same sign and related as in (12). Those errors depend on the reconstruction algorithm but if we fix one of them, the other one is determined by (12). If there is stability, the crosstalk is minimized, compare, e.g., Figure 12 and Figure 10 to Figure 8; or Figure 7 to Figure 6.

2.2.6. *Radial geometry.* Whether the Hamiltonian flow is trapping or not is not easy to verify analytically. There is one case when the Hamiltonian flow is easy to compute. Let f and a be radial, with $f(x) > 0$ in the ball $B(0,1)$, and $f = 0$ outside that ball. Then condition (10) is trivially satisfied since $W(x,\theta) = 0$ for $|x| < 1$ if and only if $x \cdot \theta = 0$. Then $\theta \cdot \partial_x W = 2f(x) > 0$ by using the transport equation. A direct calculation then shows that the Hamiltonian flow is given by

$$x = R(\sin t, \cos t), \quad \xi = \lambda(\sin t, \cos t), \quad R \geq 0,\ \lambda \neq 0. \tag{13}$$

In particular, the projections to the x-space, which we call rays, are the concentric circles $|x| = R$, $0 \leq R < 1$ (including the degenerate case of the point 0). Then no radial singularities can be recovered and all other can be recovered.

On the other hand, if we restrict the support of δa to an open set not containing any full circle $|x| = R$, $0 \leq R$, then that set is non-trapping, and we can recover $\mathrm{WF}(\delta a)$ and $\mathrm{WF}(\delta f)$ with a loss of $3/2$ derivatives. One such choice is the set $x_2 < 0$. Numerical examples illustrating that are Figure 6 and Figure 7.

2.3. **Uniqueness and stability results.** The discussion above was about the recovery of the singularities of δa and δf from the linearization. In some cases, we can derive uniqueness and stability results for the non-linear inverse problem from the results above. One needs to add a slightly stronger condition to the non-trapping one on the set K where δa can be possibly supported — pseudo-convexity: K is included in a non-trapping open set Ω and any zero bicharacteristic with endpoints over K lies over some compact set $K_1 \subset \Omega$. Below, u_0 is the solution of the transport equation (3) corresponding to a_0 and f_0, and W_0 is related to them as well.

Theorem 2.4. *Let K be a compact set and be included in a pseudo-convex $\Omega \subset \mathbf{R}^2$ w.r.t. $W_0(x, \xi^\perp)$. Let u_0 and Ba_0 be real analytic in $\Omega \times S^1$. Then for (a, f) in a C^k, $k \gg 1$, neighborhood of (a_0, f_0) with*

$$\mathrm{supp}(a - a_0) \subset K,$$

and f supported in a fixed compact set, there is uniqueness and a stability estimate of conditional Hölder type.

The next theorem states uniqueness in a small enough set under explicit conditions.

Theorem 2.5. *Let (a, f) belong to a set of smooth pairs so that* $\mathrm{supp}(a - a_0) \subset K_1$ *and* $\mathrm{supp}(f - f_0) \subset K_2$*, where K_1, K_2 are fixed compact sets. Fix $x_0 \in \mathbf{R}^2$ so that either $x_0 \notin K_2 \setminus K_1$ or* (9) *holds. Then there is a (small enough) compact set K so that if $K_{1,2} \subset K$, there is uniqueness and a stability estimate of conditional Hölder type.*

The proof of the above theorems is given in [26].

3. Methods

3.1. **Minimization.** The attenuated X-ray transform is the restriction of the solution of the PDE (3) to Γ_+. The inverse problem is: given the measurement on the boundary Γ_+, reconstruct both the source f and the attenuation a. We will design an efficient adjoint state method to solve this inverse problem in terms of transport equations; such approaches have been used in [15, 16].

To achieve this, let us define the mismatching (energy) functional

$$E(a, f; u, u^*) = \frac{1}{2} \int_{\Gamma_+} |u - u^*|^2 n \cdot \theta \, dS d\theta, \tag{14}$$

where $u^*|_{\Gamma_+}$ is the measurement on Γ_+. This energy measures the L^2-difference between the experimental measurement u^* and the solution u of the transport equation (3). We want to minimize the energy to reconstruct f and a, that is,

$$\text{Find } \{a, f\} \text{ such that } E(a, f; u, u^*) = \min_{a', f'} E(a', f'; u, u^*). \tag{15}$$

We apply the method of gradient descent to solve the optimization problem (15). We first perturb $\{a,\ f\}$ by $\{\delta a, \delta f\}$, that is,

$$a \leftarrow a + \delta a,\ f \leftarrow f + \delta f,$$

which induces the change of u by δu,

$$u \leftarrow u + \delta u.$$

Then

$$\begin{aligned} &(\theta \cdot \nabla + (a + \delta a))(u + \delta u) = f + \delta f, \\ \Rightarrow &(\theta \cdot \nabla + a)u + (\theta \cdot \nabla + a)\delta u + \delta a u + \delta a \delta u = f + \delta f, \\ \Rightarrow &(\theta \cdot \nabla + a)\delta u + \delta a u + \delta a \delta u = \delta f. \end{aligned} \tag{16}$$

After dropping the higher-order terms, we have

$$(\theta \cdot \nabla + a)\delta u + \delta a u \approx \delta f. \tag{17}$$

Then the change of the energy δE is given by,

$$\begin{aligned} & E + \delta E = \frac{1}{2} \int_{\Gamma_+} |u + \delta u - u^*|^2 n \cdot \theta \, dS d\theta \\ \Rightarrow \quad & E + \delta E = \frac{1}{2} \int_{\Gamma_+} \left(|u - u^*|^2 + 2\delta u (u - u^*) + (\delta u)^2 \right) n \cdot \theta \, dS d\theta \\ \Rightarrow \quad & \delta E = \frac{1}{2} \int_{\Gamma_+} \left(2\delta u (u - u^*) + (\delta u)^2 \right) n \cdot \theta \, dS d\theta \\ \Rightarrow \quad & \delta E \approx \int_{\Gamma_+} \delta u (u - u^*) n \cdot \theta \, dS d\theta, \end{aligned} \tag{18}$$

after dropping the higher-order terms.

Introducing the adjoint state λ, multiplying (17) by λ, taking the integral over $\Omega \times S^1$, and integrating by parts, we get

$$\begin{aligned} &(\theta \cdot \nabla + a)\delta u + \delta a u \approx \delta f, \\ &\Rightarrow \int_{\Omega\times S^1} [\lambda(\theta \cdot \nabla + a)\delta u + \lambda \delta a u]\, dx d\theta \approx \int_{\Omega\times S^1} \lambda \delta f\, dx d\theta, \\ &\Rightarrow \int_{\Gamma_+} \lambda \delta u \theta \cdot n\ dS - \int_{\Omega\times S^1} [\nabla \cdot (\theta\lambda) - a\lambda]\delta u\, dx d\theta + \int_{\Omega\times S^1} \lambda u \delta a\, dx d\theta \approx \int_{\Omega\times S^1} \lambda \delta f\, dx d\theta, \end{aligned} \tag{19}$$

that is, we have

$$\int_{\Gamma_+} \lambda \delta u \theta \cdot n\, dS - \int_{\Omega\times S^1} [\theta \cdot \nabla \lambda - a\lambda]\delta u\ dx\, d\theta + \int_{\Omega\times S^1} \lambda u \delta a\ dx\, d\theta - \int_{\Omega\times S^1} \lambda \delta f\ dx\, d\theta = 0. \tag{20}$$

Adding (18) and (20), we get

$$\begin{aligned} \delta E &- \int_{\Gamma_+} \delta u(u - u^*)\theta \cdot n dS\, d\theta + \int_{\Gamma_+} \lambda \delta u \theta \cdot n\ dS \\ &- \int_{\Omega\times S^1} [\nabla \cdot (\theta\lambda) - a\lambda]\delta u\, dx\, d\theta + \int_{\Omega\times S^1} \lambda u \delta a\, dx\, d\theta - \int_{\Omega\times S^1} \lambda \delta f\, dx\, d\theta = 0. \end{aligned} \tag{21}$$

Choosing $\lambda = \lambda(x, \theta)$ such that

$$\begin{aligned} a\lambda - \theta \cdot \nabla \lambda = 0 \quad &\text{in } \Omega, \\ \lambda = u - u^*, \ &\text{on } \Gamma_+, \end{aligned} \tag{22}$$

we have

$$\delta E = \int_{\Omega\times S^1} (\lambda \delta f - \lambda u \delta a)\ dx\, d\theta = \int_\Omega \left(\bar{\lambda}\delta f - \overline{\lambda u}\delta a\right)\ dx, \tag{23}$$

where $\bar{v} = \int_{S^1} v\, d\theta$. To minimize the energy using the method of gradient descent, we can choose the perturbations,

$$\delta f = -\bar{\lambda}, \quad \delta a = \overline{\lambda u}. \tag{24}$$

This implies,

$$\delta E = -\int_\Omega \left(\bar{\lambda}^2 + \left(\overline{\lambda u}\right)^2\right)\ dx = -\int_\Omega \left(|\delta f|^2 + |\delta a|^2\right) dx \le 0, \tag{25}$$

and the equality holds if and only if $\delta a = 0$ and $\delta f = 0$. To further regularize the perturbations, we choose the descent direction as follows: for some $\nu > 0$, we solve

$$\begin{aligned} (-\nu\Delta + 1)\delta a = \overline{\lambda u} \quad &\text{in } \Omega, \\ \delta a = 0 \quad &\text{on } \partial\Omega, \end{aligned} \tag{26}$$

and

$$\begin{aligned} (-\nu\Delta + 1)\delta f = -\bar{\lambda} \quad &\text{in } \Omega, \\ \delta f = 0 \quad &\text{on } \partial\Omega. \end{aligned} \tag{27}$$

Then we update $\{a,\ f\}$ with

$$a \leftarrow a + \delta a;\ f \leftarrow f + \delta f. \tag{28}$$

With this particular direction, we have

$$\delta E = -\int_\Omega (|\delta a|^2 + \nu|\nabla \delta a|^2)\, dx - \int_\Omega (|\delta f|^2 + \nu|\nabla \delta f|^2)\, dx \le 0, \tag{29}$$

And the equality holds when $||\delta a||_{H^1_\nu(\Omega)} = 0$ and $||\delta f||_{H^1_\nu(\Omega)} = 0$ for some weighted Sobolev space $H^1_\nu(\Omega)$.

3.2. **Minimization with constraints.** In Figure 7, we impose the constraint

$$\operatorname{supp} a \subset \bar{U},$$

where $U \subset \Omega$ is a fixed open subset. We use this to illustrate the results in Theorem 2.3 and Theorem 2.4. The modified scheme then is the following. Let $\mathbf{1}_U$ be the characteristic function of U. Then instead of (24), we choose

$$\delta f = -\bar{\lambda}, \quad \delta a = \mathbf{1}_U \overline{\lambda u}. \tag{30}$$

Then

$$\delta E = -\int_\Omega |\delta f|^2\, dx - \int_U |\delta a|^2\, dx \le 0,$$

with equality if and only if $\delta f = 0$ in Ω and $\delta a = 0$ in U.

To regularize, we solve

$$\begin{cases} (-\nu\Delta + 1)\phi = \overline{\lambda u} & \text{in } U, \\ \phi = 0 & \text{on } \partial U, \end{cases} \tag{31}$$

and set

$$\delta a = \begin{cases} \phi, & \text{in } U, \\ 0 & \text{in } \Omega \setminus U. \end{cases}$$

Then

$$\delta E = -\int_U (|\delta a|^2 + \nu|\nabla \delta a|^2)\, dx - \int_\Omega (|\delta f|^2 + \nu|\nabla \delta f|^2)\, dx \le 0, \tag{32}$$

and this turns into an equality if and only if $\delta f = 0$ in Ω and $\delta a = 0$ in U.

3.3. **Discretization.** The discretization of the above algorithm is implemented as follows. Let us assume that there are N directions: $\{\theta_i : i = 1, 2, \dots, N\}$. Each of them is associated with a measurement u_i^* for $i = 1, 2, \dots, N$. The energy is

$$E^N(a, f; \{u_i\}_1^N, \{u_i^*\}_1^N) = \sum_{i=1}^N \int_{\Gamma^+_{\theta_i}} |u_i - u_i^*|^2 dS, \tag{33}$$

where u_i is the solution of (3) corresponding to θ_i for $i = 1, 2, \dots, N$, and

$$\Gamma^\pm_{\theta_i} = \{x \in \partial\Omega :\ \pm\theta_i \cdot n(x) \ge 0\},$$

The perturbation of the energy is given by

$$\delta E^N = \sum_{i=1}^N \left\{ \int_\Omega \lambda_i \delta f\ d\Omega - \int_\Omega \lambda_i u_i \delta a\, dx \right\}, \tag{34}$$

which is slightly different from (23). Here λ_i is the adjoint variable of u^i for $i = 1, 2, \ldots, N$, solving

$$\begin{aligned} a\lambda_i - \nabla \cdot (\theta_i \lambda_i) &= 0 \quad \text{in } \Omega, \\ \lambda_i \theta_i \cdot n &= u_i - u^* \quad \text{on } \partial\Omega^+_{\theta_i}. \end{aligned} \tag{35}$$

We choose the regularized direction as

$$\delta a = (-\nu\Delta + 1)^{-1} \left\{ \sum_{i=1}^{N} \lambda_i u_i \right\}, \ \delta f = (-\nu\Delta + 1)^{-1} \left\{ \sum_{i=1}^{N} -\lambda_i \right\} \tag{36}$$

with a properly chosen regularization parameter $\nu > 0$. Finally, we update $\{a, f\}$ as

$$a \leftarrow a + \delta a, \ f \leftarrow f + \delta f;$$

see also (24).

3.4. **Algorithm.** We summarize an algorithm for the inverse attenuated X-ray problem.

Algorithm for inverse attenuated X-ray problem.

(1) Initialization of $\{a^k, f^k\}$ for $k = 0$ (refer to examples in Section 4).
(2) Compute $\{u_i\}_{i=1}^N$ by solving (3) with $\{\theta_i\}_{i=1}^N$ using $\{a^k, f^k\}$.
(3) Obtain $\{\lambda_i\}_{i=1}^N$ by solving (35).
(4) Obtain $\{\delta a^k, \delta f^k\}$ using (36).
(5) Determine step size ϵ^k using, for example, the Armijo-Goldstein (AG) rule or simply choosing $\epsilon^k = \epsilon$ for given ϵ.
(6) Update
$$a^{k+1} = a^k + \epsilon^k \delta a^k; \ f^{k+1} = f^k + \epsilon^k \delta f^k.$$
(7) Repeated from Step 2 until $||\delta a^k|| \leq \delta_0$ and $||\delta f^k|| \leq \delta_0$, or $k \geq k_{max}$, where δ_0 and k_{max} are given convergence criteria.

In Step 2 and Step 3, both equations are solved with the fast sweeping method[14, 15, 16, 29]. In Step 4, a fourth order solver with the fast Fourier transform (FFT) is used to solve the elliptic equation. The L-BFGS quasi-Newton method is applied to speed up the iterations for solving the optimization problem (15). In the L-BFGS code, the gradient descent direction is computed with the above adjoint state approach.

4. Numerical Examples

We present numerical examples to demonstrate the proposed method and the theoretical understanding of the problem. Our examples also demonstrate the importance of the non-trapping condition and the importance of the real non-degeneracy conditions (9) and (10). In particular, the latter determine what part of the wave front set of f and a can be reconstructed, assuming smooth background a and f, based on the linearization, see Theorem 2.2, and Theorem 2.3 but we test this for the non-linear problem.

4.1. **Robustness of the method.** We start with an example showing the performance of the method with a good initial guess.

Figure 3. In this example, $a_0 = 0$ and $f_0 = 1$ which are represented by the black color in the pictures below (notice the different gray scales used for a and f). The Hamiltonian is not even C^1 here because f_0 is not zero near the corners. As we can see the reconstruction is good, in general. Aside from the points and directions determining lines hitting one of the corners, the non-degeneracy condition (9) is fulfilled everywhere except for x on one of the coordinate axes and θ perpendicular to it. At those points, however, condition (10) holds, so the real principal type property still holds, which in particular excludes open instability sets like in Section 4.4 below.

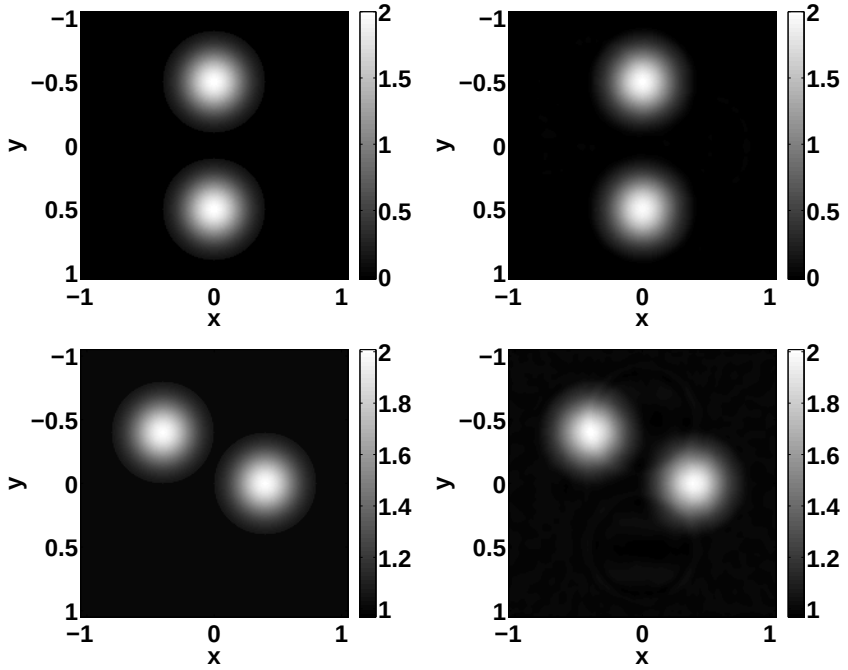

FIGURE 3. "Good guess" $a_0 = 0$, $f_0 = 1$. Top row: a, bottom row: f. First column: exact a and f; second column: computed with those guesses.

In contrast, if we use a constant approximation for the attenuation and try to recover f only, the reconstruction is quite bad; see Figure 4.

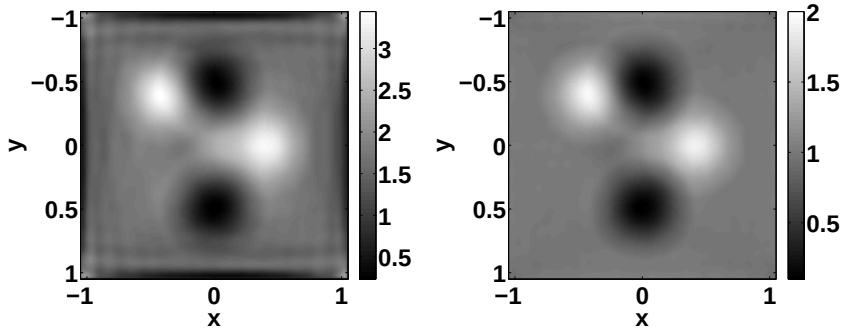

FIGURE 4. A reconstruction attempt of f in Figure 3 with a constant (and kept fixed). (a) $a = 0$, (b) $a = 0.5$.

4.2. **Ill-posedness in elliptically symmetric geometry.**

Figure 5. In addition to the spherical non-uniqueness example in Figure 1, we get numerical non-uniqueness for (a, f) with level curves consisting of concentric ellipses. The results are presented in Figure 5. While one can show that the Hamiltonian flow is trapping and the rays consist of those ellipses, there is no known non-uniqueness theorem in this case.

Perturbing them with small non-"elliptic" δa, δf produces results (not shown here) similar to those in Figure 2.

4.3. **Trapping geometry.** The next two examples are intended to show the ill-posedness with trapping geometry and how we can stabilize the problem by using the a priori knowledge that the perturbations are supported in a non-trapping domain. The initial guesses are not "good", as in Figure 3. On the other hand, with "good" guesses, the reconstructions would be similar to those there. Notice that in Figure 1, Figure 2 and Figure 5, the geometry is trapping already.

Figure 6. The background functions a_0 and f_0 are $a_0 = 0$ and f_0 equal to the characteristic function of the unit disk. They are radial, and different initial guesses lead to circular artifacts because the errors propagate along the rays (the circles $|x| =$ const. in this case). The initial guesses for a are like the original a but with (guessed) phantoms shifted upward and with different amplitudes. The attenuation a (more precisely, its X ray transform) is too small to affect significantly the reconstruction of f in this case. Notice the different gray scales on the first row, chosen so that the negative values can be displayed.

Figure 7. In the next experiment, we use the a priori knowledge that a is supported in the lower half of the square, which is non-trapping because it contains no complete circle. The recovery is shown in Figure 7. The support constraint stabilizes the problem. This example and the previous one illustrate Theorem 2.4.

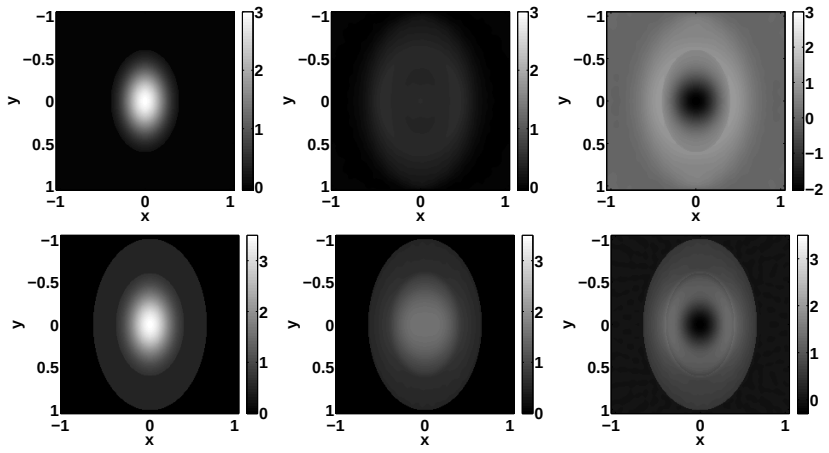

FIGURE 5. Apparent non-uniqueness for "elliptic" (a, f). Top row: a, bottom row: f. First column: exact a and f; second and third columns: computed with different initial guesses.

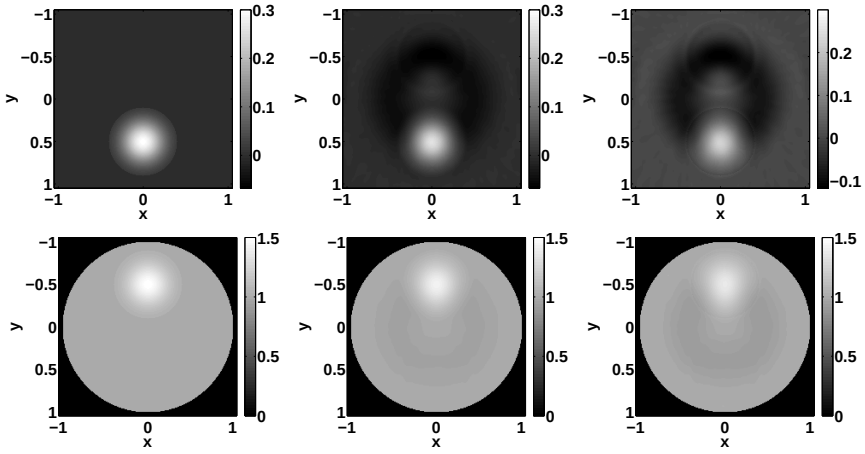

FIGURE 6. Ill posedness with circular rays. Top row: a, bottom row: f. First column: exact a and f; second and third column: computed with different guesses. The artifacts are circular, dictated by the Hamiltonian flow.

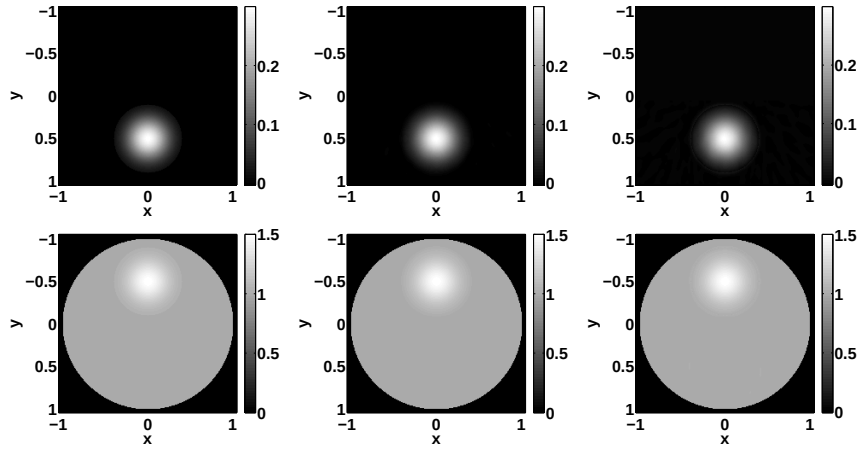

FIGURE 7. Stabilized example with circular rays. A constraint condition for $\operatorname{supp} a$ to be in $y < 0$ was used. The initial guesses were the same as in Figure 6. Top row: a, bottom row: f. First column: exact a and f; second column: computed with guess 1; third column: computed with guess 2.

4.4. **Open characteristic (instability) set.** In the next examples, W has an open set of zeros (x, θ), and therefore the Hamiltonian $W(x, \xi^{\perp})$ has an open set of characteristic points (zeros) and co-directions (x, ξ) at them. The real principal type condition (10) does not hold anymore. This creates microlocal instability and one cannot recover the wave front set at such (x, ξ). This instability is much stronger than in the trapping but still of real principal type case where the characteristic variety is a codimension-one submanifold.

Figure 8. In the next two examples, the source f is represented by four "walls" near the border of the computational region. We choose $f = 1$ there, and $f = 0$ zero otherwise. There is a large open set in the phase space consisting of x between the "walls" and θ such that the line determined by

(x, θ) intersects the "walls" at both ends at opposite sides but not too close to the corners. If the line intersects two adjacent sides (away from some neighborhood of the corners again), W has a simple zero when the slope is ± 1. If x is close to the center, then such lines form a small set, and W vanishes for a large set of directions θ not too close to one of the two diagonals. This creates strong instability for the linearization. This is illustrated in the lower left sub-figure of Figure 8: integrals of f along the dotted and along the solid rays, for each such line, are equal.

The recovery is shown in Figure 8. The results depend strongly on the number N of directions used, and on the solver used. With the L-BFGS solver, the recovered a takes values in the range $(-0.31, 0.70)$ instead of $(0, 1)$, while with the AG solver (the gradient descent solver with the AG step-size rule), that range is $(-0.25, 0.34)$. On the other hand, the two solvers show very similar results in more stable and even in milder unstable cases. Note that the initial guesses are "good" but the reconstruction is still poor. The artifacts in the reconstructed f in the form of a dark phantom mirroring that in a, are quite strong.

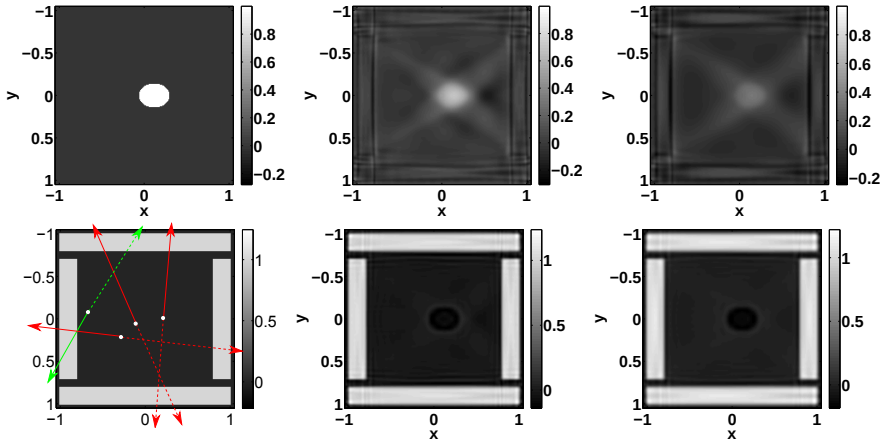

FIGURE 8. A large open set of unstable points. Top row: a, bottom row: f. First column: exact a and f; second column: computed with guess zero for both a and f with the LBFGS solver; third column: computed with guess zero for both a and f with the AG solver.

Figure 9. In the next example, we moved the phantom closer to one of the corners. The set of points and directions corresponding to zeros of W shrinks, and as a consequence, stability increases. The stable lines actually appear in the reconstruction as faint brighter lines connecting the phantom and some small neighborhoods of the corners. There is still an open set over the phantom where $W = 0$ and the problem is still very unstable. The results are shown in Figure 9 and the rays in the bottom left sub-figure have the same meaning as in Figure 8; they represent unstable directions.

Figure 10. We choose a as in the previous example but we remove two "walls" from f. This changes the determinant W drastically. Integrals of u along opposite rays vanish in a much smaller angle now; see Figure 11. In Figure 11, one such line is the one hitting the left and the bottom sides, while the lines hitting the top side are "stable" (in green) — integrals are zero in one of the directions and are positive in the opposite directions, hence $W \neq 0$ there. We still have $W = 0$ in an open set in the phase space but that set is smaller than before. As a result, the artifact in the reconstructed f — the oval caused by the corresponding oval in a, has more contrast along the

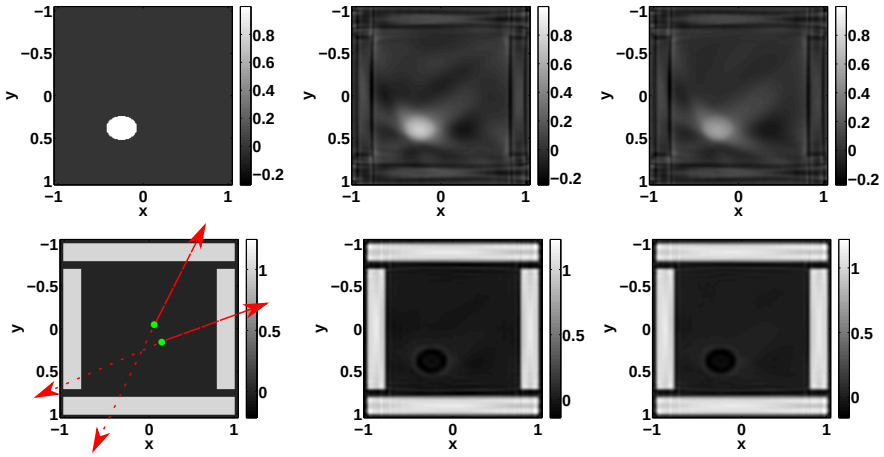

FIGURE 9. The phantom was moved closer to a corner compared to the previous example. This decreases the set of the unstable points (the zeros of W). Top row: a, bottom row: f. First column: exact a and f; second column: computed with guess zero for both a and f with the LBFGS solver; third column: computed with guess zero for both a and f with the AG solver.

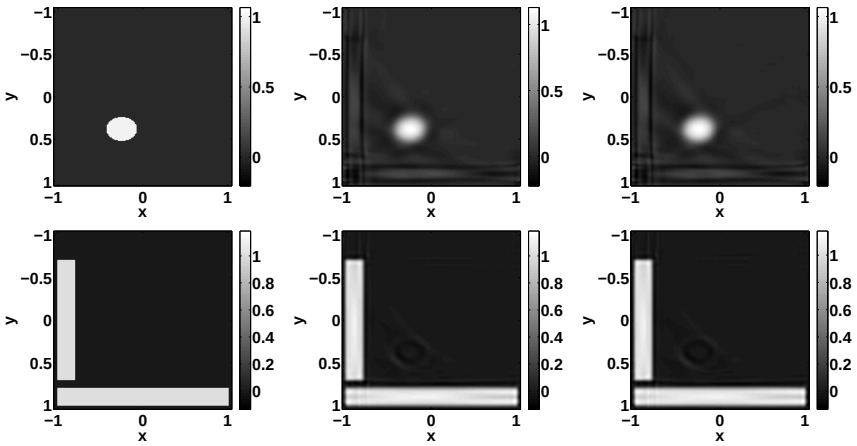

FIGURE 10. Two "walls" removed. For computed a, $(\min a, \max a) = (-0.2041, 1.0638)$. The non-trapping set is smaller, hence better stability. First column: exact a and f; second column: computed with guess zero for both a and f with the LBFGS solver; third column: computed with guess zero for both a and f with the AG solver.

edges having slopes close to 1. Those are the unstable (co-)directions, and since the contrast should be zero, this is where the error maximizes. On the other hand, near the edges with slope close to -1, the contrast is lower, i.e., closer to the truth. In contrast, in Figure 9, the same artifact in the recovery of f is stronger, with approximately uniform edges.

Figure 12. In this example, f has the same support as in Figure 9, the same average value but the amplitude increases linearly in the direction $(-1, 1)$, see Figure 13, where the stable lines are in green, and the stable co-directions are normal to them; and the unstable lines are in red, with

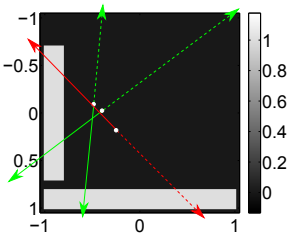

FIGURE 11. In Figure 10, we have a smaller but still open instability set represented here by the line with negative slope.

unstable co-directions normal to them again. As a result, for all lines not intersecting the square close to the corners, condition (9) is satisfied, and for each x between the walls, there are two (opposite) directions where $W = 0$. The unstable (co-)directions are the ones along $\pm(-1, 1)$ and those close to these two directions because of a small denominator. The most stable ones are the ones close to $\pm(1, 1)$. As a result, in the third picture in the first row in Figure 12, the reconstructed a with the AG solver, the contrast along the edges of the phantom normal to $\pm(1, 1)$ is best reconstructed. Since this configuration is more stable than the one in Figure 9, the artifacts in the reconstructed f are much less pronounced.

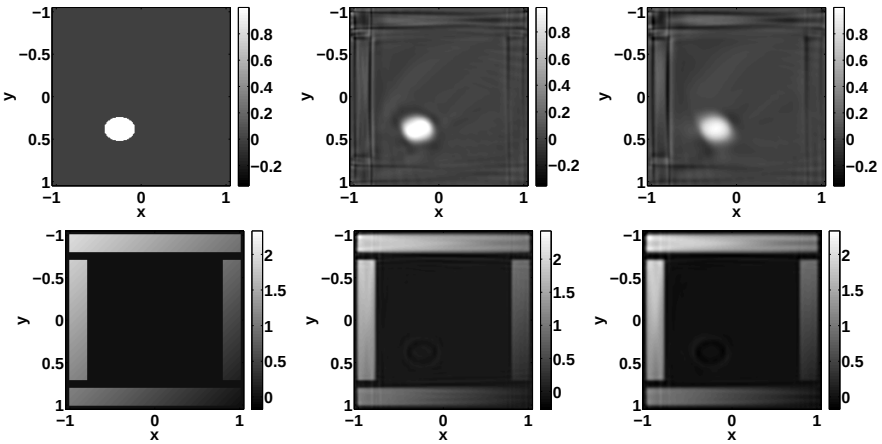

FIGURE 12. Back to four "walls" but with linearly changing density of f along the direction $(-1, 1)$. The zeros of W are (almost) a set of lower dimension: two opposite θ's at each x. First column: exact a and f; second column: computed with guess zero for both a and f with the LBFGS solver; third column: computed with guess zero for both a and f with the AG solver.

5. CONCLUSION

Motivated by recent theoretical results obtained by the third author for the identification problem arising in single-photon emission computerized tomography (SPECT), we designed an adjoint state method for recovering both the source and the attenuation in the attenuated X-ray transform. Our starting point is the transport-equation characterization of the attenuated X-ray transform, and we apply efficient fast sweeping methods to solve static transport equations and adjoint state

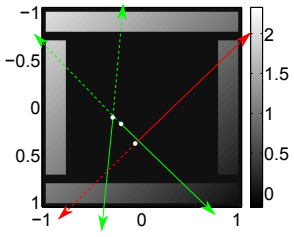

FIGURE 13. In Figure 12, for x between the walls, there are two instability directions corresponding here to the line with slope approximately 1.

equations. Numerous examples are presented to demonstrate various features of the identification problem, such as uniqueness and non-uniqueness, stability and instability, and propagation of wave front sets. Future work includes a three-dimensional implementation of the method.

References

[1] È. V. Arbuzov, A. L. Bukhgeim, and S. G. Kazantsev. Two-dimensional tomography problems and the theory of A-analytic functions [translation of *Algebra, geometry, analysis and mathematical physics (Russian) (Novosibirsk, 1996)*, 6–20, 189, Izdat. Ross. Akad. Nauk Sibirsk. Otdel. Inst. Mat., Novosibirsk, 1997];. *Siberian Adv. Math.*, 8(4):1–20, 1998.

[2] G. Bal and A. Jollivet. Combined source and attenuation reconstructions in SPECT. *preprint*, 2011.

[3] J. Boman. On generalized Radon transforms with unknown measures. In *Integral geometry and tomography (Arcata, CA, 1989)*, volume 113 of *Contemp. Math.*, pages 5–15. Amer. Math. Soc., Providence, RI, 1990.

[4] A. V. Bronnikov. Numerical solution of the identification problem for the attenuated Radon transform. *Inverse Problems*, 15(5):1315–1324, 1999.

[5] A. V. Bronnikov. Reconstruction of attenuation map using discrete consistency conditions. *IEEE Trans. Med. Imaging*, 19(5):451–462, 2000.

[6] A. A. Bukhgeim and S. G. Kazantsev. Inversion formula for the Fan-Beam attenuated Radon transform in a unit disk. *Sobolev Institute of Mathematics, Siberian Branch of Russian Acad. Sci., Novosibirsk*, preprint No. 99, 2002.

[7] A. L. Bukhgeim. Inverse gravimetry approach to attenuated tomography. In *Tomography and inverse transport theory*, volume 559 of *Contemp. Math.*, pages 49–63. Amer. Math. Soc., Providence, RI, 2011.

[8] Y. Censor, D. E. Gustafson, A. Lent, and H. Tuy. A new approach to the emission computerized tomography problem: Simultaneous calculation of attenuation and activity coefficients. *IEEE Trans. Nucl. Sci.*, 26(2):2775–2779, 1979.

[9] N. Dencker. On the propagation of polarization sets for systems of real principal type. *J. Funct. Anal.*, 46(3):351–372, 1982.

[10] V. Dicken. A new approach towards simultaneous activity and attenuation reconstruction in emission tomography. *Inverse Problems*, 15:931–960, 1999.

[11] D. Finch. The attenuated x-ray transform: recent developments. In *Inside Out, Inverse Problems and Applications*, pages 47–66. Mathematical Sciences Research Institute Publications, Edited by G. Uhlmann, Cambridge University Press, 2003.

[12] D. Gourion and D. Noll. The inverse problem of emission tomography. *Inverse Problems*, 18(5):1435–1460, 2002.

[13] L. Hörmander. *The analysis of linear partial differential operators. IV*, volume 275. Springer-Verlag, Berlin, 1985. Fourier integral operators.

[14] C. Y. Kao, S. J. Osher, and J. Qian. Lax-Friedrichs sweeping schemes for static Hamilton-Jacobi equations. *J. Comput. Phys.*, 196:367–391, 2004.

[15] S. Leung and J. Qian. An adjoint state method for three-dimensional transmission traveltime tomography using first-arrivals. *Comm. Math. Sci.*, 4:249–266, 2006.

[16] S. Luo, S. Leung, and J. Qian. An adjoint state method for numerical approximation of continuous traffic congestion equilibria. *Comm. in Computational Physics*, 10:1113–1131, 2011.

[17] S. H. Manglos and T. M. Young. Constrained intraspect reconstruction from spect projections. In *Proc. IEEE Conf Nuclear Science Symp. and Medical Imaging Conf. Record*, pages 1605–1609, 1993.

[18] F. Natterer. The identification problem in emission computed tomography. In *Mathematical aspects of computerized tomography (Oberwolfach, 1980)*, volume 8 of *Lecture Notes in Med. Inform.*, pages 45–56. Springer, Berlin, 1981.

[19] F. Natterer. Computerized tomography with unknown sources. *SIAM J. Appl. Math.*, 43(5):1201–1212, 1983.

[20] F. Natterer. Inversion of the attenuated Radon transform. *Inverse Problems*, 17(1):113, 2001.

[21] R. G. Novikov. An inversion formula for the attenuated X-ray transformation. *Ark. Mat.*, 40(1):145–167, 2002.

[22] R. G. Novikov. On the range characterization for the two-dimensional attenuated x-ray transformation. *Inverse Problems*, 18(3):677–700, 2002.

[23] R. Ramlau and R. Clackdoyle. Accurate attenuation correction in spect imaging using optimization of bilinear functions and assuming an unknown spatially-varying attenuation distribution. In *Proc. Conf Nuclear Science Symp. Record. 1998 IEEE*, volume 3, pages 1684–1688, 1998.

[24] H. Rullgård and E. T. Quinto. Local Sobolev estimates of a function by means of its Radon transform. *Inverse Probl. Imaging*, 4(4):721–734, 2010.

[25] D. C. Solmon. The identification problem for the exponential Radon transform. *Math. Methods Appl. Sci.*, 18(9):687–695, 1995.

[26] P. Stefanov. The identification problem for the attenuated x-ray transform. *preprint*.
[27] A. Welch, R. Clack, F. Natterer, and G. T. Gullberg. Toward accurate attenuation correction in SPECT without transmission measurements. *IEEE Trans. Med. Imaging*, 16(5):532–541, 1997.
[28] H. Zaidi and B. Hasegawa. Determination of the attenuation map in emission tomography. *J Nucl Med*, 44(2):291–315, 2003.
[29] H. K. Zhao. Fast sweeping method for eikonal equations. *Math. Comp.*, 74:603–627, 2005.

Department of Mathematics, Iowa State University, Iowa State University, Ames, IA 50011

Department of Mathematics, Michigan State University, East Lansing, MI 48824.

Department of Mathematics, Purdue University, West Lafayette, IN 47907